Structural disorder of ball-milled, nanosized, Fe-doped SnO_2: X-ray diffraction and Mössbauer spectroscopy characterization

Thiago S. Ribeiro · José M. Sasaki · Igor F. Vasconcelos

Abstract Structural characterization of nanosized Fe-doped semiconducting oxide SnO_2 is reported. Samples of $Sn_{1-x}Fe_xO_{2-y}$ (with x ranging from 0.11 to 0.33) were processed in a planetary ball mill, subsequently HCl-washed to eliminate metallic iron impurities introduced by the milling tools, and characterized by X-ray diffraction and Mössbauer spectroscopy. Results showed that Fe enters the host matrix randomly replacing Sn in octahedral sites regardless of iron concentration. It has been found the presence of oxygen deficient iron sites attributed to the stoichiometric unbalance of precursor materials used in the milling process. It is known that structural features like particle size and residual microstrain are highly affected by the milling process. Values of average particle sizes as calculated by Scherrer's method alone decreased with increasing Fe concentration. This result was shown, by means of the Williamson-Hall correction method, to be misleading as a large degree of microstrain is expected for mechanically milled powders. In fact, corrected values of average particle sizes turned out to be reasonably homogeneous regardless of iron content and milling time with no consistent trend. Residual microstrain, on the other hand, was found to increase with iron content giving way to the conclusion that broadening of diffraction peaks are mostly due to increasing microstrain as a function of iron doping

and milling time. Williamson-Hall analysis also showed a large degree of particle size inhomogeneity. Milling of undoped SnO_2 showed that this inhomogeneity is due mostly to doping as opposed to milling.

Introduction

Although most oxides are good insulators, some are semiconductors like CuO, Cu_2O, SnO_2, ZnO, amongst others. Semiconducting oxides present many aspects of technological appeal, and therefore, they attract the interests of scientists and engineers. New growth techniques allow these oxides to be used as host compounds for the production of magnetic semiconductors [1]. Magneto-optical devices and spintronics-based technologies are likely the most promising applications of magnetic semiconducting oxides. Specifically, development and functionalization of magnetic semiconductors are key to spintronics which explores the possibility of using electron spins in electronic devices for processing, transferring, and storing of information. Many of such applications would require a combination of semiconducting and magnetic properties in the same material [2]. Room temperature ferromagnetism is a preferred property for these magnetic semiconductors, which can be achieved in many oxide semiconductors when doped with a magnetic ion, like Co-doped CeO_2 [3] and SnO_2 [4]. In short, combination of semiconductivity and magnetism in the same class of material opens up a realm of possibilities in the device technology [1].

Tin dioxide (SnO_2) has many technological applications due to properties like transparency in the visible region of the electromagnetic spectrum and high thermal stability. This compound is used in many fields which include

T. S. Ribeiro · I. F. Vasconcelos (✉)
Departamento de Engenharia Metalúrgica e de Materiais, Universidade Federal do Ceará, Campus do Pici Bloco 714, Fortaleza, CE 60455-760, Brazil
e-mail: ifvasco@ufc.br

J. M. Sasaki
Departamento de Física, Universidade Federal do Ceará, Fortaleza, CE, Brazil

development and fabrication of electronic and optical devices [5], solar cells [6–8], liquid crystal displays [9], gas sensors [10], and batteries [11]. SnO_2 has a rutile-like tetragonal crystal structure where Sn^{+4} ions occupy octahedral sites, while O^{-2} ions occupy plane trigonal sites. Fe-doped SnO_2 is a magnetic semiconductor with chemical formula $Sn_{1-x}Fe_xO_2$, where x is the amount of doping. Fe^{+3} has a similar ionic radius as Sn^{4+} (0.64 and 0.69 Å, respectively) making substitutional doping possible. Because tin ions have a higher valence than iron ions, Fe impurities play the role of receptor, making it a type-p semiconductor [12].

Nanostructured powders of $Sn_{1-x}Fe_xO_2$ have been successfully prepared by various techniques, such as high-energy ball milling [13–17], Pechini [10], hydrothermal methods [18–20], polymeric precursors method [10, 21, 22], and sol–gel [17, 23–26]. Paramagnetic [18, 27] and ferromagnetic [23, 26, 27] properties are found in the $Sn_{1-x}Fe_xO_2$ compound. According to Thurber et al. [26], the ferromagnetic nature of $Sn_{0.95}Fe_{0.05}O_2$ nanopowders is inversely proportional to the oxygen concentration in the synthesis environment. Bilovol et al. [27] suggest that the ferromagnetism in these materials may be associated to α-Fe impurities. On the other hand, Nomura et al. [23] claim the material presents a very complex ferromagnetism behavior that depends on the synthesis method and is related to the interaction between ferroic ions but also to magnetic defects.

High-energy ball milling carries a number of advantages over other techniques as it is a fast, simple, low-cost, and low-maintenance technique. Nevertheless, this technique has a few drawbacks like the high amounts of impurities and disorder, and defects introduced in the material. Sanchez et al. [16, 17] report the synthesis of Fe-doped SnO_2 by mechanical milling. They were, however, not able to obtain pure $Sn(Fe)O_2$ as iron impurities remain in the powder. Another group of researchers managed to produce pure mechanically milled $Sn(Fe)O_2$ [13–15] but with a large amount of Fe^{+2}, as determined by Mössbauer spectroscopy, which may be an indication of the existence of another iron phase not detected by X-ray diffraction. All the previous studies on this subject have not been able to fully address the important fact of structural disorder and defects introduced by the milling process. This knowledge may come down to be detrimental to the actual technological usefulness of ball-milled $Sn_{1-x}Fe_xO_2$ as disorder and defects are expected to influence the physical properties of these materials. This study attempts to fill in this void by presenting this much needed approach. Grain size, microstrain, and Fe coordination in high-energy ball-milled Fe-doped SnO_2 (x ranging from 0.11 to 0.33) were studied by X-ray diffraction and Mössbauer spectroscopy.

Experimental procedure

Samples of $Sn_{1-x}Fe_xO_{2-y}$ were prepared by high-energy ball milling. Commercial SnO_2 and Fe_2O_3 (Sigma-Aldrich, purity $\geq 99.9\%$) powders, and steel vials and balls (ball-to-powder mass ratio of 20:1) were used in a Fritsch Pulverissette 6 planetary mill operating with an angular velocity of 500 rpm. According to Sorescu et al. [19], the solubility of Fe_2O_3 in SnO_2 imposes a limit to the iron content of approximately $x = 0.30$. In this way, samples with $x = 0.11$ through $x = 0.33$, as determined by X-ray fluorescence spectroscopy, were prepared. Doping of SnO_2 with Fe_2O_3 causes an oxygen deficiency introducing an uncertainty on the concentration $2 - y$ of this element. Undoped commercial SnO_2 without milling and after being milled for 3 h were also analyzed to provide a basis for comparison.

Similar reaction kinetics of Fe_2O_3 incorporation by SnO_2, as the milling time elapsed, was observed regardless of iron concentration, as monitored by X-ray diffraction and Mössbauer spectroscopy. The major difference recorded was regarding the duration of reaction: the larger the iron concentration the longer the milling time taken to complete the incorporation, i.e., from 2 h for $x = 0.11$ to 4 h for $x = 0.33$.

The last sample of each time series was selected to be HCl washed [28] to remove metallic iron impurities introduced during the milling process. The samples were then washed with distilled water to remove the excess of HCl and dried at temperature of 100 °C for a period of 24 h.

X-ray diffraction patterns were collected at room temperature using a Panalytical Xpert Pro MPD diffractometer operating with a Kα-Co source ($\lambda = 1,788965$ Å) at 40 kV and 40 mA. The high-resolution diffraction is obtained with a hybrid monochromator for incidence beam, which consists of parabolic mirror and Ge monochromator producing a parallel and highly monochromatic beam. The data were collected with Pixcel, Panalytical 2nd generation solid-state detection technology.

Rietveld refinement procedures were applied to all the X-ray patterns using DBWSTools 2.3 [29] software based on the standard crystal structure of SnO_2 (ICSD-39173). Particle sizes were estimated by Scherrer's relation and corrected by the Williamson-Hall method [30] which separates contributions of particle size and residual microstrain to the breadth of diffraction peaks.

The width of a diffraction peak is affected by both the average particle size and the residual microstrain. The average particle size D contribution (β_D) to the width of a diffraction peak is described by Scherrer's equation (disregarding microstrain and inhomogeneity):

$$D = \frac{k\lambda}{\beta_D \cos\theta}, \quad (1)$$

where λ is the radiation wavelength, θ is the diffraction angle, and k is a constant related to the shape of particles ($k = 1$ for spherical particles). On the other hand, the contribution β_ϵ of residual microstrain ($\epsilon = \frac{\Delta d}{d}$, where d is the interplanar space) to the width of a diffraction peak is described by the relation of Stokes and Wilson [31]:

$$\beta_\epsilon = 4\epsilon \tan\theta. \quad (2)$$

Combining the contributions of average particle size in Eq. 1 and residual microstrain in Eq. 2 to the peak width yields the Williamson-Hall relation [30]:

$$\frac{\beta\cos\theta}{\lambda} = \frac{k}{D} + \frac{4\epsilon}{\lambda}\sin\theta, \quad (3)$$

where β is the measured peak width, corrected for instrumental line broadening.

Equation 3 can be fitted to experimental data (plotted as $\sin\theta \times \frac{\beta\cos\theta}{\lambda}$) to obtain D and ϵ through the linear and angular coefficients, $\frac{k}{D}$ and $\frac{4\epsilon}{\lambda}$, respectively. This is true provided particle sizes are homogeneous in all crystallographic directions, and thus, the experimental data fall into a straight line as described by the Williamson-Hall relation.

Room temperature Mössbauer spectra were measured in transmission mode using a ^{57}Co(Rh) radioactive source mounted on a velocity driver operating in sinusoidal mode. Powdered samples were inserted in an acrylic sample holder with a 0.5-cm central round slot. A lead mask was used to collimate the beam. Transmitted photons were collected by an ion chamber operating in the proportional counter mode while the spectra were counted and defined by a multi-channel analyzer synchronized to the velocity driver. The data were evaluated by least square fitting to series of discrete Lorentzian-shaped subspectra by means of the software package Normos. Isomer shifts (δ) are quoted with respect to α-Fe.

## Results and discussion

As mentioned in the previous section, similar reaction kinetics of Fe_2O_3 incorporation by SnO_2 was observed for all values of x. To show all the data would be redundant and thus only the data for $x = 0.18$ is presented and discussed.

X-ray patterns for samples with $x = 0.18$ milled for 0, 0.5, 1, 2, 3, and 4 h are shown in Fig. 1a. The diffractogram for the 0-h sample showed peaks relative to both the SnO_2 and Fe_2O_3 phases. After 0.5 h, Fe_2O_3 peaks are no longer distinguishable suggesting complete incorporation. Expected broadening of peaks due to reduction of particle size and increase of microstrain is also observed.

Figure 1b shows the Mössbauer spectra for these samples together with best fits to the data. The reaction can be clearly depicted by the appearance of a central doublet (blue subspectrum) with hyperfine parameters (not shown)

Fig. 1 (color online) **a** X-ray diffraction patterns with best Rietveld fits and **b** Mössbauer spectra with best fits to the data, of milled $Sn_{1-x}Fe_xO_{2-y}$ $x = 0.18$
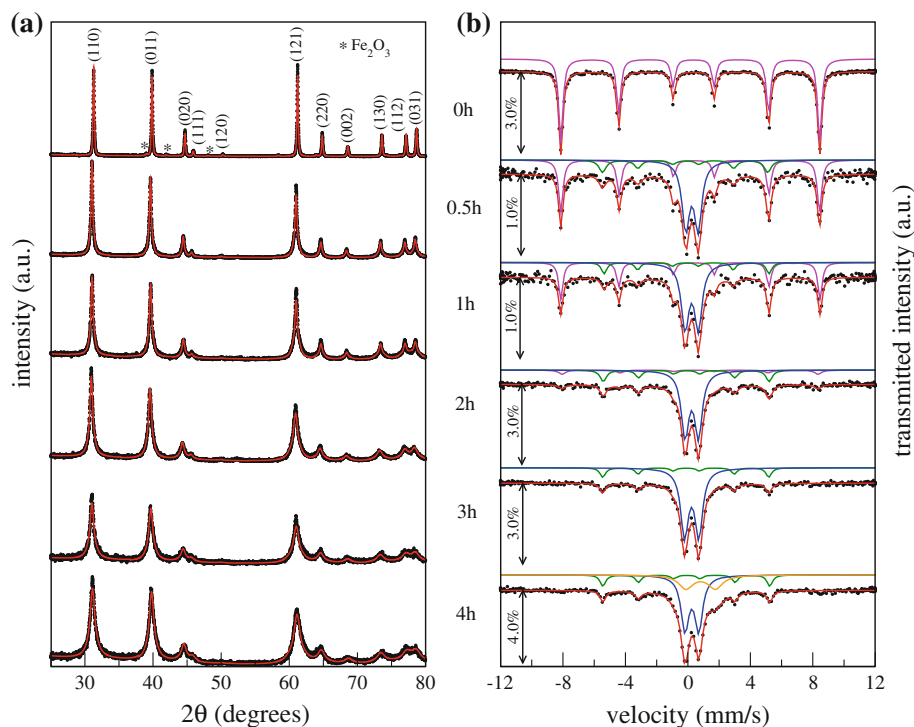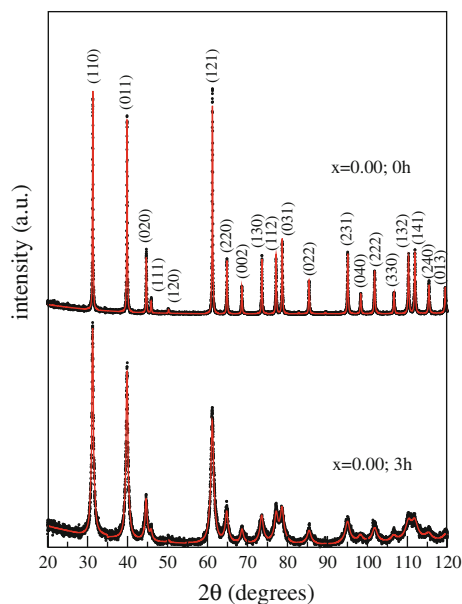
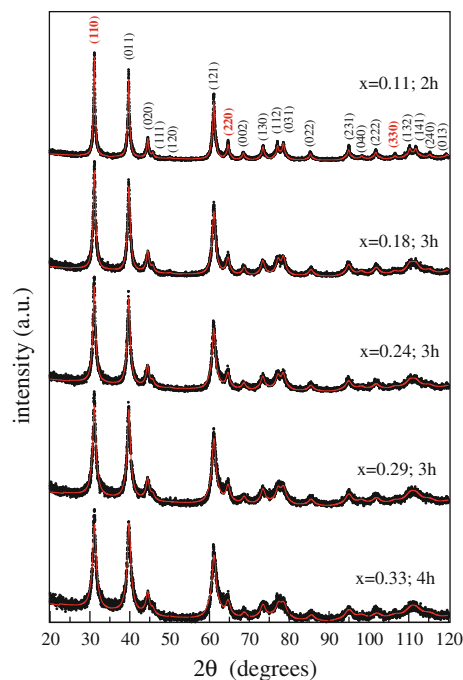**Fig. 2** (color online) X-ray diffraction patterns for undoped SnO_2, unmilled, and milled for 3 h

Fig. 3 (color online) X-ray diffraction patterns for HCl-washed $Sn_{1-x}Fe_xO_{2-y}$ with best Rietveld fits to the data (*red lines*)

Fig. 4 (color online) Williamson-Hall plots for undoped (*red curves*) and doped (*black curves*) samples

consistent with octahedrally coordinated Fe^{+3}, at the expense of the Fe_2O_3 sextet (magenta subspectrum). The reaction was already underway after 0.5 h but not yet completed, in contrast to what was suggested by the analysis of the X-ray patterns. In fact, Fe_2O_3 incorporation by SnO_2 is not completed before 3 h of milling, which is close to an optimum time, as formation of an unpreferred Fe-bearing phase is observed after milling for 4 h (orange doublet). It has been found that the optimum milling time is a function of iron concentration and increases from 2 h for $x = 0.11$ to 4 h for $x = 0.33$.
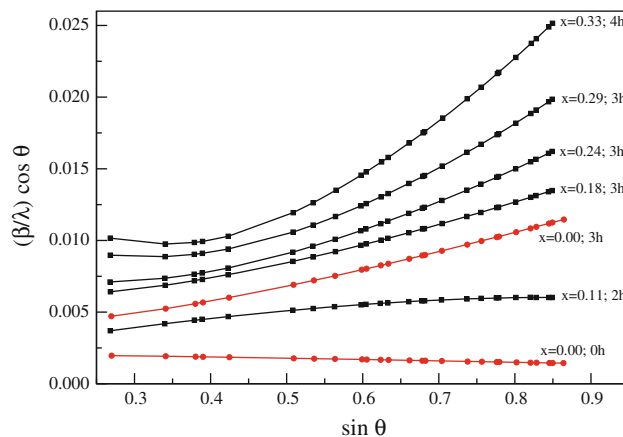
The local nature of Mössbauer spectroscopy allows for identification of minority phases that X-ray diffraction fails to detect. Besides failing to detect Fe_2O_3 after 0.5 h of milling, X-ray patterns also did not show the presence of α-Fe impurities for all the milling times (green sextets in Mössbauer spectra). Chosen samples for each iron composition were HCl washed and further analyzed.

X-ray diffraction patterns for undoped SnO_2 (unmilled and milled for 3 h) are shown in Fig. 2 while patterns for ball-milled samples of $Sn_{1-x}Fe_xO_{2-y}$ are shown in Fig. 3. Peaks of SnO_2 (ICSD-39173) are the only ones present in all the patterns. Moreover, Fe doping, regardless of concentration, has not affected the diffraction patterns indicating random incorporation of Fe into the SnO_2 matrix.

Williamson-Hall plots are shown in Fig. 4. Curves for the undoped SnO_2 samples (red curves in the Fig. 4) are linear, indicating homogeneous particle size distributions. The larger slope of the 2-h curve reflects the introduction of microstrain as an effect of milling. Black curves in the figure suggest that incorporation of Fe in the host SnO_2

matrix leads to inhomogeneity in particle size distribution. The larger the doping percentage, the more inhomogeneous the particle size distribution, as seen by the consistent departure from linearity of the black curves in Fig. 4. It is important to stress that these results suggest that inhomogeneity is mostly a consequence of doping and not milling time, most likely due to the slightly smaller ionic radius of Fe^{+3}.

In light of this inhomogeneity, average particle size was calculated for the {110} family of planes represented by the (110), (220), and (330) reflections, indicated in Fig. 3.
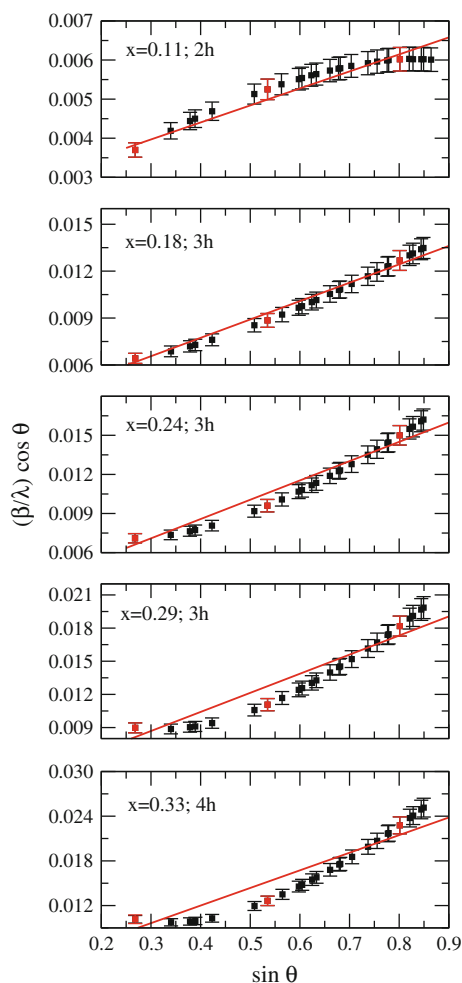
Fig. 5 (color online) Detailed Williamson-Hall plots for HCl-washed $Sn_{1-x}Fe_xO_{2-y}$ showing the best linear fits to the three points corresponding to the {110} family of planes

Williamson-Hall plots for the doped samples are shown in more detail in Fig. 5, together with uncertainties and the best linear fit to the three points corresponding to the (110), (220) and (330) reflections.

Table 1 shows results of Rietveld refinement and Williamson-Hall correction for the diffraction patterns. The unit cell volume decreases slightly with Fe content since its ionic radius (0.64 Å) is smaller than that of Sn (0.69 Å),

indicating incorporation of Fe as a substitutional doper. Values of average particle sizes as calculated by Scherrer's method alone (D_S in Table 1) decrease with increasing Fe concentration.

This result is misleading as a large degree of microstrain is expected for mechanically milled powders, which is confirmed by the Williamson-Hall corrected values. In fact, corrected values of average particle sizes (D_{WH} in Table 1) are reasonably homogeneous, regardless of iron content and milling time with no consistent trend. Residual microstrain, on the other hand, increases with doping giving way to the conclusion that broadening of diffraction peaks are mostly due to increasing microstrain as a function of iron content.

High degrees of disorder and defects introduced by the milling process give rise to non-homogeneous particle shape and size distributions yielding nonlinear Williamson-Hall plots. As a matter of fact, the higher the doping percentage, the more nonlinear is the Williamson-Hall plot as can be seen in Fig. 5. Linear fits to these nonlinear data carry inherently large uncertainties, even when the {110} family of planes alone are considered in the fits. The effect is more noticeable in the corrected average particle size uncertainties as, for sample with $x = 0.24$, the uncertainty is of 15.7 nm which is about one half the value of D_{WH} (see Table 1), whereas, for samples with $x = 0.29$ and $x = 0.33$, the three points do not even fall on a straight line even when error bars are considered (see Fig. 5). Uncertainties of D_{WH} for these samples are of the same order of magnitude as D_{WH} itself, rendering the fitted values unreliable. Despite this shortcoming, it is still important to point out the importance of using a correction method like Williamson-Hall when interpreting the breadth of diffraction peaks taken from high-energy milled samples to avoid underestimating of particle sizes.

Mössbauer spectra of HCl-washed samples and respective best fits are shown in Fig. 6, while hyperfine parameters are presented in Table 2. Best fits were achieved using two doublets, and the absence of sextets confirms the successful incorporation of Fe to the matrix and removal of metallic iron impurities by the HCl washing procedure. Isomer shift and quadrupole splitting values of both

Table 1 Structure of unit cell ($\alpha = \beta = \gamma = 90°$) alongside with particle sizes as given by Scherrer's relation (D_S) and Williamson-Hall method (D_{WH}) and residual microstrain (ϵ) for the {110} family of planes

Sample	$a = b$ (Å)	c (Å)	vol (Å^3)	D_S (nm)	D_{WH} (nm)	ϵ (%)
$x = 0.00$; 3 h	4.7395(2)	3.1843(2)	71.53(7)	14.8(4.0)	62.90(6.0)	0.500(1)
$x = 0.11$; 2 h	4.7387(3)	3.1831(2)	71.47(1)	18.6(2.4)	37.60(6.9)	0.190(4)
$x = 0.18$; 3 h	4.7392(6)	3.1785(5)	71.43(1)	10.1(1.6)	33.00(9.6)	0.520(6)
$x = 0.24$; 3 h	4.7385(7)	3.1765(5)	71.41(1)	09.1(1.6)	37.7(15.7)	0.66(14)
$x = 0.29$; 3 h	4.7374(8)	3.1769(6)	71.35(2)	07.6(1.3)	–	0.77(24)
$x = 0.33$; 4 h	4.7397(5)	3.1731(8)	71.25(2)	06.5(1.3)	–	1.06(37)
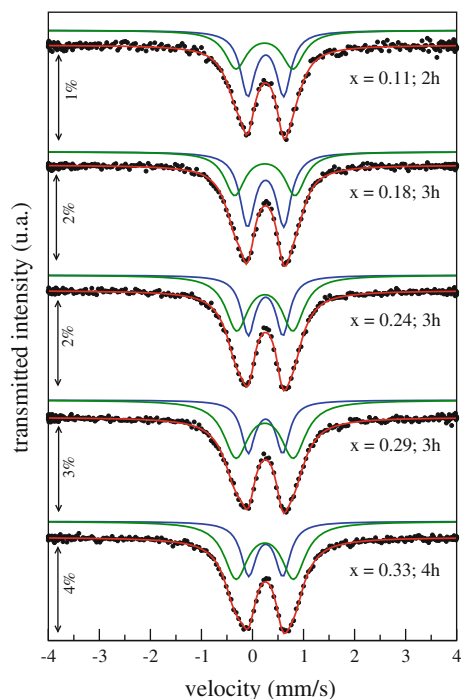
Fig. 6 (color online) Mössbauer spectra for HCl-washed $Sn_{1-x}Fe_xO_{2-y}$ with best fits to the data: doublet 1 (*blue line*) and doublet 2 (*green line*)

Table 2 Hyperfine parameters obtained from fits to Mössbauer spectra

Sample	Doublet 1				Doublet 2			
	δ	Δ	Γ	Area (%)	δ	Δ	Γ	Area (%)
$x = 0.11$; 2 h	0.37	0.70	0.35	54(5)	0.34	1.12	0.51	46(6)
$x = 0.18$; 3 h	0.37	0.71	0.36	55(3)	0.35	1.18	0.48	45(3)
$x = 0.24$; 3 h	0.37	0.68	0.33	41(3)	0.35	1.10	0.52	59(3)
$x = 0.29$; 3 h	0.37	0.67	0.32	34(4)	0.35	1.12	0.58	66(4)
$x = 0.33$; 4 h	0.37	0.67	0.35	37(3)	0.35	1.13	0.56	63(4)

δ, Δ and Γ in mm/s. Uncertainties of δ, Δ and Γ values smaller than 0.02 mm/s

doublets are consistent with octahedral coordinated Fe^{+3} substituting for Sn^{+4} in the SnO_2 [19] matrix confirming successful doping as suggested by the X-ray diffraction results.

Larger values of quadrupole splitting found for doublet 2 are attributed to oxygen-deficient octahedral iron sites. In fact, oxygen-deficient octahedra carry enlarged electric field gradients and consequently larger values of quadrupole splitting [14]. Moreover, relative spectral areas show an increase in the number of oxygen-deficient sites with doping and milling times (Table 2). This is associated to the disorder induced by increasing doping and milling times and by the oxygen unbalanced stoichiometry introduced by the doping of SnO_2 with Fe_2O_3.

Conclusions

Doping of SnO_2 with Fe_2O_3 by high-energy ball milling was successfully achieved for various degrees of doping. X-ray diffraction patterns of $Sn_{1-x}Fe_xO_{2-y}$ confirmed that, for $x = 0.11$ through $x = 0.33$, only one phase with the SnO_2 structure is present in all the samples. Moreover, Fe-doping, regardless of concentration, has not affected the diffraction patterns indicating the random incorporation of Fe into the SnO_2 matrix as a substitutional doper. The absence of Fe_2O_3 peaks suggests that the reaction was complete and the absence of metallic iron peaks confirms that the HCl wash procedure was successful to remove Fe impurities with no structural changes.

Mössbauer measurements confirm the incorporation of Fe into the SnO_2 matrix as a substitutional doper as isomer shift, and the quadrupole splitting values of doublets obtained from the fits are consistent with octahedral-coordinated Fe^{+3} substituting for Sn^{+4} in the SnO_2 structure. The best fit is achieved with two doublets instead of one, and larger values of quadrupole splitting found for the second doublet are attributed to oxygen-deficient octahedral iron sites, as doping of SnO_2 with Fe_2O_3 causes an oxygen unbalanced stoichiometry. This unbalance is confirmed by an increase in this second doublet's relative spectral area with doping fraction and milling time.

High-energy ball milling is an efficient, fast, and low-cost technique for synthesizing various kinds of powdered materials. However, the technique carries disadvantages—the most remarkable being the large amounts of impurities and disorder introduced in the material. Structural features like particle size and residual microstrain are highly affected by the milling process. In the literature, particle sizes are broadly determined by Scherrer's method with no regards for the fact that both particle size and residual microstrain contribute to the widths of diffraction peaks.

It has been shown in this contribution that, when dealing with mechanically milled samples, Scherrer's method alone is not adequate, as a correction is needed to account for residual microstrain contributions to the width of diffraction peaks. Williamson-Hall correction, although appropriate up to a certain degree of disorder, does not provide a definitive method for separating these two contributions, as it fails to properly correct particle sizes for

highly inhomogeneous samples. Despite this shortcoming, it is still important to point out the importance of using a correction method when interpreting the breadth of diffraction peaks taken from high-energy milled samples to avoid underestimating of particle sizes.

References

1. Fukumura F, Toyosaki H, Yamada Y (2005) Semicond Sci Technol 20:S103
2. Furdyna JK, Schiffer P, Sasaki Y, Potashnik SJ, Liu XY (2000) In: Sadowski ML, Potemski M, Grynberg M (eds) Optical properties of semiconductor nanostructures. Kluwer Academic Publishers, Dordrecht , p 221
3. Colis S, Bouaine A, Moubah R, Schmerber G, Ulhaq-Bouillet C, Dinia A, Daharon L, Petersen J, Becker C (2010) J Appl Phys 108:0539101
4. Xu Y, Tang Y, Li C, Cao G, Ren W, Xu H, Ren Z (2009) J Alloy Compd 481:837
5. Prellier W, Fouchet A, Mercey B (2003) J Phys-Condens Mat 15:R1583
6. Bak YR, Kim GO, Hwang MJ, Cho KK, Kim KW, Ryu KS (2011) J Sol-Gel Sci Technol 58:518
7. Li B, Luo L, Xiao T, Hu X, Lu L, Wang J, Tang Y (2011) J Alloy Compd 509:2186
8. Im JS, Park S, Jeon JW, Lim KS (2011) Sol Energ Mat Sol C 95:150
9. Kolentsov K, Yourukova L, Zheliaskova A, Rachkova A (2004) Bulg J Phys 31:87
10. Vaishampayan MV, Deshmukh RG, Walke P, Mulla IS (2008) Mater Chem Phys 109:230
11. Du N, Zhang H, Chen B, Ma X, Huang X, Tu J, Yang D (2009) Mater Res Bull 44:211
12. Galatsis K, Cukrov L, Wlodarski W, McCormick P, Kalantarzadeh K, Comini E, Sberveglieri G (2003) Sensor Actuat B Chem 93:562
13. Cabrera AF, Mudarra-Navarro AM, Rodriguez-Torres CE, Sanchez FH (2007) Physica B 398:215
14. Torres CER, Cabrera AF, Sanchez FH (2007) Physica B 389:176
15. Bilovol V, Mudarra-Navarro AM, Cabrera AF, Rodriguez-Torres CE, Sanchez FH (2007) Hyperfine Interact 179:381
16. Sanchez LC, Calle AM, Arboleda JD, Osorio J, Nomura K, Barrero CA (2008) Microeletron J 39:1320
17. Sanchez LC, Beltran JJ, Osorio J, Calle AM, Barrero CA (2010) Hyperfine Interact 195:185
18. Fang L, Zu X, Liu C, Li Z, Peleckis G, Zhu S, Liu H, Wang L (2010) J Alloy Compd 491:679
19. Sorescu M, Diamandescu L, Tarabasanu-Mihaila D, Teodorescu VS, Howard BH (2004) J Phys Org Chem 65:1021
20. Liu JF, Lu MF, Chai P, Fu L, Wang ZL, Cao XQ, Menga J (2007) J Magn Magn Mat 317:1
21. Sakuma J, Nomura K, Barrero C, Takeda M (2007) Thin Solid Films 515:8653
22. Beltran JJ, Sanchez LC, Osorio J, Tirado L, Baggio-Saitovitch EM, Barrero CA (2010) J Mater Sci 45:5002. Doi:10.1007/s10853-010-4454-z
23. Nomura K, Barrero C, Sakuma J, Takeda M (2006) Czech J Phys 56:75
24. Rani S, Roy SC, Kararc N, Bhatnagar MC (2007) Solid State Commun 141:214
25. Rani S, Roy SC, Bhatnagar MC (2007) Sensor Actuat B Chem 122:204
26. Thurber A, Reddy KM, Punnoose A (2009) J Appl Phys 105:07E706
27. Bilovol V, Navarro AMM, Torres CER, Sanchez FH, Cabrera AF (2009) Physica B 404:2834
28. Xiaoyan P, Dongmei J, Yan L, Xeuming M (2006) J Magn Magn Mater 305:388
29. Bleicher L, Sasaki JM, Paiva-Santos CO (2000) J Appl Crystallogr 33:1189
30. Williamson GK, Hall WH (1953) Acta Metall Mater 1:22
31. Stokes AR, Wilson AJC (1943) Proc Cambridge Phil Soc 40:197